

Improving the energy uniformity for large liquid scintillator detectors

Guihong Huang^{a,b}, Yifang Wang^a, Wuming Luo^{a,*}, Liangjian Wen^{a,*}, Zeyuan Yu^a, Weidong Li^a, Guofu Cao^a, Ziyan Deng^a, Tao Lin^a, Jiaheng Zou^a, Miao Yu^c

^aInstitute of High Energy Physics, Chinese Academy of Sciences, Beijing 100049, China

^bSchool of Physical Sciences, University of Chinese Academy of Science, Beijing 100049, China

^cWuhan University, Wuhan 430072, China

Abstract

It is challenging to achieve high precision energy resolution for large liquid scintillator detectors. Energy non-uniformity is one of the main obstacles. To surmount it, a calibration-data driven method was developed previously to reconstruct event energy in the JUNO experiment. In this paper, we investigated the choice of calibration sources thoroughly, optimized the calibration positions and corrected the residual detector azimuthal asymmetry. All these efforts lead to a reduction of the energy non-uniformity near the detector boundary, from about 0.64% to 0.38%. And within the fiducial volume of the detector it is improved from 0.3% to 0.17%. As a result the energy resolution could be further improved.

Keywords: JUNO, Liquid scintillator detector, Neutrino experiment, Energy reconstruction, Energy uniformity

1. Introduction

Liquid scintillator (LS) detectors with ultra-low background have been widely used in neutrino experiments. Just to name a few: KamLAND [1], Borexino [2], Double Chooz [3], Daya Bay [4] and RENO [5]. Instead of dwelling on the outstanding scientific achievements made by these experiments in recent decades [6–10], and how LS detectors will continue to play a crucial role in neutrino physics in the future, let us do a quick comparison of the LS detectors from above. The detector size varies from 10 tons to 10^3 tons in target mass, and the detector energy resolution ranges from 5% to 8%. On the other hand JUNO [11] will be the largest LS detector in the world with a target mass of 20 kton upon completion, and its designed energy resolution is $\sim 3\%/\sqrt{E}$, which is much more precise with respect to earlier experiments. Even though it is rather challenging to achieve such high precision energy resolution for a large LS detector, a comprehensive calibration program [12] demonstrated that the required energy resolution of JUNO could be achieved, by accurately modeling the energy non-linearity and correcting for the energy non-uniformity. The residual non-uniformity in [12] is less than 0.3% within the fiducial volume of the detector. Since the energy resolution has such significant impact, and one of the main contributing factors is the energy non-uniformity, we wanted to further reduce it, especially for regions near the detector boundary which amounts to more than 20% of the whole detector volume.

Due to the complicated optical processes, an optical model independent method [13] was developed previously to reconstruct the energy of positrons from inverse β -decay (IBD) events

in the Central Detector (CD) of JUNO. The basic idea is to construct the maps of expected photoelectrons (PEs) for Photomultiplier tubes (PMTs) from calibration data, and then use these maps to build a maximum likelihood function to reconstruct the event energy. In this paper we will further improve the energy uniformity in the CD of JUNO, by taking into account the asymmetry of a realistic detector and optimizing the calibration strategy. Due to lack of real data, Monte Carlo (MC) simulation data generated by JUNO offline software [14] are used instead. The ideas and methods discussed here are also applicable to other experiments using large LS detectors.

The structure of this paper is as follows: in Sec. 2, we will briefly describe the CD of JUNO and its calibration systems. All the MC samples used will be listed in Sec. 3. From Sec. 4 to Sec. 6, we will present an update on the maps of expected PEs, a thorough study on the calibration sources, and an optimization on calibration points respectively. In Sec. 7 we will discuss the residual energy non-uniformity. And finally we will give the summary in Sec. 8.

2. JUNO CD and Calibration Systems

A schematic view of the CD and the calibration system of JUNO is shown in Fig. 1. The CD is made up of an acrylic sphere which has a diameter of 35.4 m and contains 20,000 ton LS. The acrylic sphere is supported by a stainless-steel latticed shell (SSLS) via acrylic nodes and connecting bars. The diameter of the SSLS is 40.1 m, and the gap between it and the acrylic sphere is filled with pure water. About 17,600 20-inch PMTs and 25,600 3-inch PMTs are installed on the stainless-steel shell to collect photons. Given the different refractive indices of LS and water, refraction and total reflection could occur during photon propagation. JUNO also has a complex calibration

*Corresponding author

Email addresses: luowm@ihep.ac.cn (Wuming Luo), wenlj@ihep.ac.cn (Liangjian Wen)

system [12] which consists of four sub-systems, namely the Automated Calibration Unit (ACU), the Cable Loop System (CLS), the Guide Tube (GT) and the remotely operated vehicle (ROV). Only the former three are used for energy reconstruction in this paper. It should be emphasized that each sub-system could cover a different detector region: ACU can move along the Z-axis of the CD, CLS is able to reach those points permitted by the mechanics of the loop system within X-Z plane. GT is mounted on the outer surface of the acrylic sphere, designed to calibrate the detector in the edge region complementary to ACU and CLS.

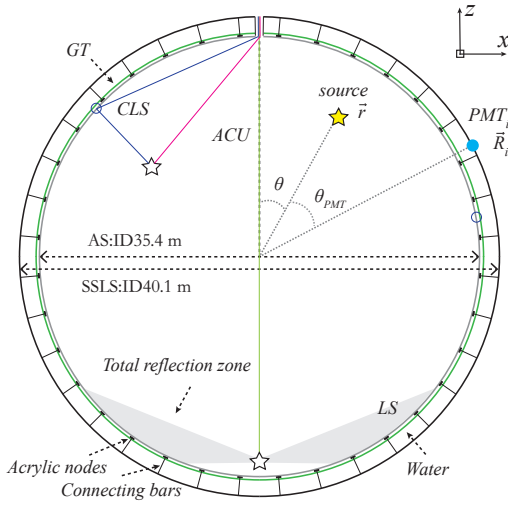


Figure 1: Schematic view of the CD and the calibration system. Z-axis is the vertical central axis of the CD. An example of total reflection is also shown at the bottom. Upper-Right: definition of the three parameters of $\hat{\mu}$ in Sec. 4. \vec{r} is the calibration source position, \vec{R}_i is the i^{th} PMT position and θ_{PMT} is the angle between \vec{r} and \vec{R}_i .

3. Monte Carlo Samples

Various calibration data samples with different sources taken from Ref. [12] are produced. For the prompt signal of IBD events, a set of positron samples are also prepared. The information of the calibration samples and the positron samples used in this paper are summarized in Tab. 1 and Tab. 2, respectively. For all these samples, the detector simulation is done based on Geant4 [15]. LS properties [16] and optical processes of photons propagating in LS are implemented [17, 18]. Realistic detector geometry such as the arrangement of the PMTs and the supporting structures is also deployed. For simplicity the electronics simulation which includes various PMT characteristics is disabled.

The calibration samples are used to construct the maps of expected PEs per unit energy for PMTs, referred to as $\hat{\mu}$ hereafter and described in detail in Sec. 4. Calibration sources with different types and energies are compared in order to select the most suitable one. Nine sets of positron samples with kinetic

energy $E_k = (0, 1, 2, \dots, 8)$ MeV are used to evaluate the performance of energy reconstruction. The events in each positron sample are uniformly distributed in the CD.

Table 1: Information of the calibration samples. ^{68}Ge is a positron emitter, the kinetic energy of the positrons will be absorbed by the source enclosure, so only the annihilation gammas are released. For the Laser source, “op” stands for optical photon and 1 MeV corresponds to 11522 optical photons. The event statistics per position is 10k.

Source	Type	Energy [MeV]	N_{position}	Stats./pos.
^{68}Ge	γ	2×0.511	2000	10k
^{60}Co	γ	$1.173 + 1.333$	275	10k
AmC	(n,H) γ	2.22	275	10k
Laser	op	1	2000	10k

Table 2: List of the positron samples.

Source	Kinetic energy	Statistics/MeV	Position
e^+	(0,1,2, ..., 8) MeV	450k	uniform in CD

4. Energy Reconstruction and $\hat{\mu}$

As described in Ref. [13], an optical model independent method was developed to reconstruct the energy of positrons in the JUNO CD. The observables for each positron are $\{k_i\}$, where k_i represents the number of detected PEs for the i^{th} PMT and is expected to follow a Poisson distribution. The mean value of the Poisson distribution μ_i is the product of the positron visible energy E_{vis} and $\hat{\mu}_i$ from Sec. 3. So the probability of observing $\{k_i\}$ for all PMTs can be constructed as Eqn. 1 when an event deposits energy at position (r, θ, ϕ) .

$$\mathcal{L}(\{k_i\}|r, \theta, \phi, E_{\text{vis}}) = \prod_i \mathcal{L}(k_i|r, \theta, \phi, E_{\text{vis}}) = \prod_i \frac{e^{-\mu_i} \cdot \mu_i^{k_i}}{k_i!} \quad (1)$$

$$\mu_i = E_{\text{vis}} \cdot \hat{\mu}_i$$

where the index i runs over all PMTs. After obtaining $\hat{\mu}_i$, the event energy can be fitted by maximizing this likelihood function. In order to decouple the influence of the vertex uncertainty on the energy reconstruction, the event vertex is assumed to be known in this study.

The key component of the energy reconstruction method discussed above is $\hat{\mu}$. In Ref. [13], it is derived from the ACU calibration data, under the assumption that the JUNO CD has good spherical symmetry. If the calibration source position is defined as $\vec{r} = (r, \theta, \phi = 0)$ and the i^{th} PMT position as \vec{R}_i , as shown in Fig. 1, then $\hat{\mu}$ can be calculated as:

$$\hat{\mu}(r, \theta_{PMT}) = \frac{\mu(r, \theta_{PMT})}{E_{\text{vis}}} = \left(\frac{1}{M} \sum_{i=1}^M \frac{\bar{n}_i}{DE_i} \right) \cdot \frac{1}{E_{\text{vis}}} \quad (2)$$

$$E_{\text{vis}} = PE_{\text{total}}/Y_0$$

where E_{vis} is the visible energy of the calibration source, PE_{total} is the total number of PEs, Y_0 is the constant light yield defined in Ref. [12], the index i runs over the PMTs with the same θ_{PMT} , \bar{n}_i is the average number of detected PEs and DE_i is the relative detection efficiency. Given there are only finite ACU calibration positions, $\hat{\mu}(r = z, \theta_{PMT})$ from these positions are extrapolated through linear interpolation to the entire (r, θ_{PMT}) phase space.

Fig. 2 compares the $\hat{\mu}(r, \theta_{PMT})$ maps for calibration positions with the same radius but different θ angle, as could be collected by the CLS calibration sub-system. The apparent differences, which are mainly caused by the shadowing effect of the acrylic nodes and connecting bars when θ varies, indicate that the detector is not symmetric along the θ direction, and this θ dependence for $\hat{\mu}(r, \theta_{PMT})$ must be taken into account. Since the CLS system can move in the X-Z plane, we could combine the CLS and ACU calibration data to construct $\hat{\mu}(r, \theta, \theta_{PMT})$ in the same way as before.

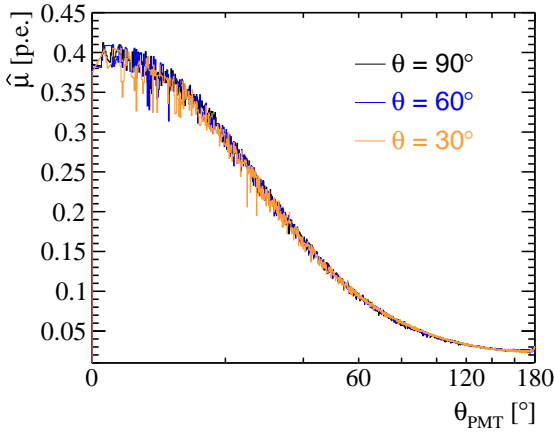


Figure 2: Comparison of $\hat{\mu}$ for calibration positions with different θ angle and fixed radius $r = 10$ m. The spikes are mainly caused by the shadowing effect of the acrylic nodes and connecting bars. The unit of $\hat{\mu}$ is p.e. which stands for 1 photon electron.

A few examples of the $\hat{\mu}(r, \theta, \theta_{PMT})$ maps at fixed θ_{PMT} values are shown in Fig. 3. And they are also affected by the same shadowing effect. The Delaunay triangles based cubic spline interpolation has been applied to $\hat{\mu}(r, \theta, \theta_{PMT})$, so that it could be extrapolated to the whole (r, θ) phase space from finite calibration positions. At this point, it is quite natural to ask whether there is any ϕ dependence for $\hat{\mu}$, which could be caused by any detector asymmetry along the ϕ direction. We will leave this discussion to Sec. 7.

5. Comparison of Calibration Sources

Our energy reconstruction method heavily relies on the usage of calibration data. Given all the available calibration sources, which one gives the best energy reconstruction performance? Bearing this question in mind, we thoroughly investigated these sources: other than the energy, what else could be different for these sources? How do the $\hat{\mu}$ maps compare? And eventually how does the energy reconstruction performance compare?

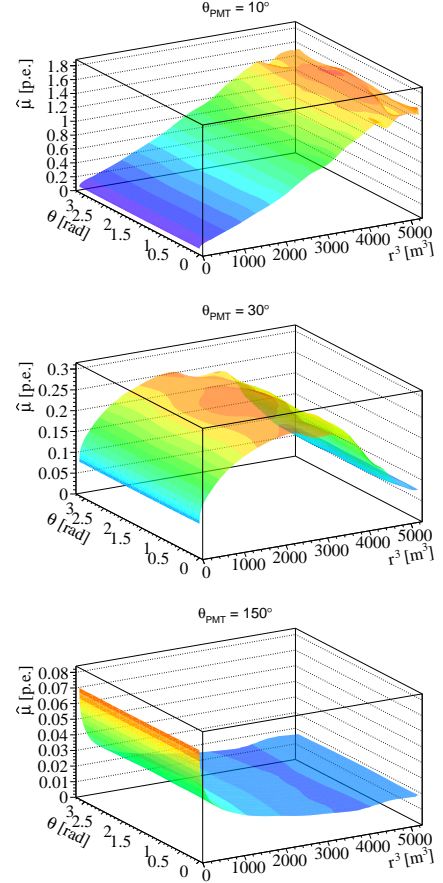


Figure 3: Examples of the $\hat{\mu}(r, \theta, \theta_{PMT})$ maps at three θ_{PMT} angles.

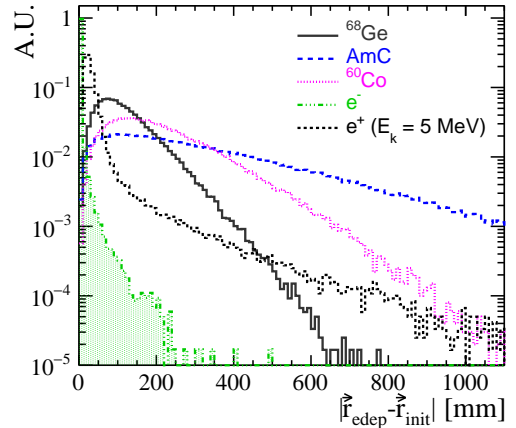


Figure 4: Distribution of the distance ΔR between energy-deposit center \vec{r}_{edep} and initial calibration position \vec{r}_{init} for different sources. A hypothetical position source with $E_k = 5$ MeV is also drawn for comparison.

In Fig. 4 we compared the distribution of the distance ΔR between energy-deposit center \vec{r}_{edep} and initial calibration position \vec{r}_{init} for different sources. Laser source is set to be point-like in the MC simulation, and in reality it is approximately point-like due to the diffuse ball which absorbs the optical photons from Laser and re-emits them isotropically [19]. For illustra-

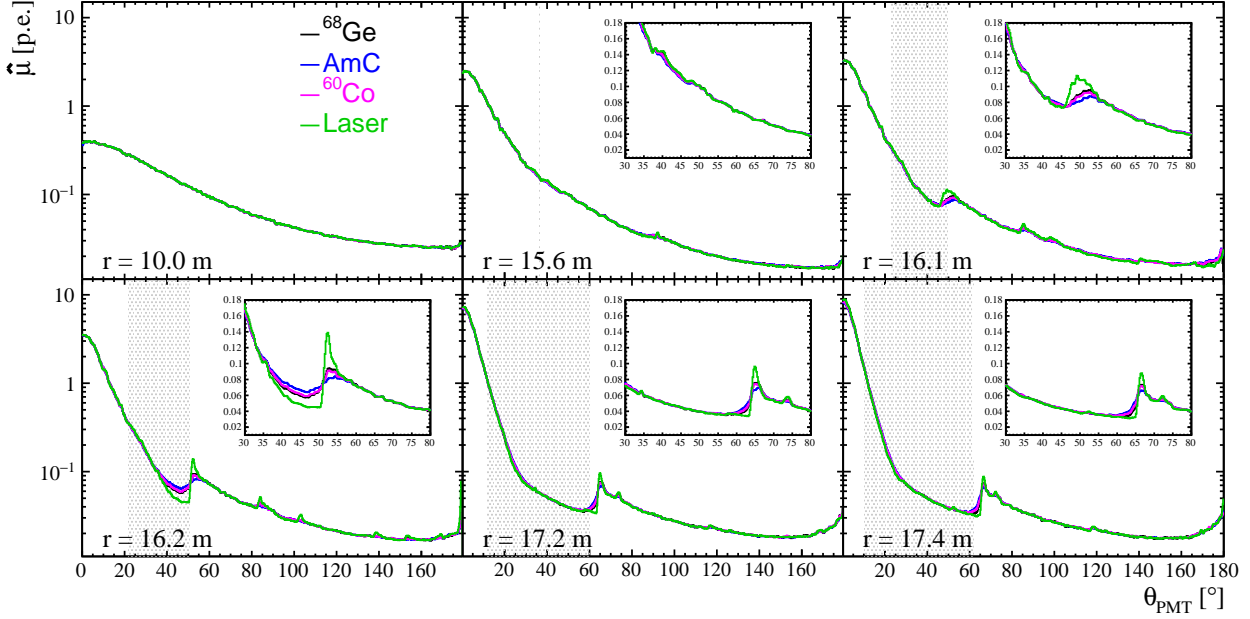


Figure 5: Comparison of $\hat{\mu}$ for different sources at a few representative calibration positions. From left to right and top to bottom, $r = (10, 15.6, 16.1, 16.2, 17.2, 17.4)$ m, $\theta = 90^\circ$, $\phi = 0^\circ$. The shaded region indicates the total reflection zone.

tion purpose, a virtual mono-energetic electron source is depicted instead of Laser. A hypothetical position source with $E_k = 5$ MeV is also drawn for comparison. Electron source is very close to point-like and \vec{r}_{dep} is almost identical to \vec{r}_{init} . While for the gamma sources there is a clear deviation of \vec{r}_{dep} from \vec{r}_{init} , since a gamma deposits its energy in LS mainly through multiple Compton scattering. For ^{68}Ge source, the two gammas from positron-electron annihilation tend to be back to back directionally. On the other hand, ^{60}Co radiates two gammas (1.173 MeV and 1.333 MeV) without any direction correlation, leading to a wider spread of ΔR . AmC is a neutron source, the neutron will travel some distance before being captured by hydrogen and then emitting a 2.22 MeV photon, thus its ΔR has the widest spread among all the sources.

The CD is divided into regions I, II and III: namely the central region ($r < 15.6$ m), the total reflection region ($15.6 \text{ m} < r < 17.2$ m) and the outer-FV (fiducial volume) region ($17.2 \text{ m} < r$), and six representative calibration positions are picked: $r = (10, 15.6, 16.1, 16.2, 17.2, 17.4)$ m, $\theta = 90^\circ$, $\phi = 0^\circ$. The comparison of the $\hat{\mu}$ maps among different sources at these points is shown in Fig. 5. The $\hat{\mu}$ maps had been smoothened and it was checked that this smoothening has negligible impact on the energy reconstruction. A few observations immediately stand out:

1. In region I, the $\hat{\mu}$ maps are nearly monotonic and also similar for all sources.
2. In regions II and III, the $\hat{\mu}$ maps have a kink. And there are noticeable discrepancies among the sources around the kink.

In region I where the sources are relatively far away from the PMTs, all sources could be approximately regarded as point-like, thus leading to similar $\hat{\mu}$ maps. Moreover, since total reflection won't occur in region I, as θ_{PMT} increases, smaller solid angle leads to decreased $\hat{\mu}$. While in regions II and III, there is always a total reflection zone for any given source position, mainly due to the refractive index mis-match between LS ($n = 1.496@430$ nm) and water ($n = 1.353@430$ nm). An example is shown in Fig. 1. For those PMTs in the total reflection zone (as indicated by the shadowed region in the plots), one would expect a large decrease of detected PEs due to photon redistribution and loss. In addition ΔR also becomes relevant for these PMTs, because any small deviation of the source position would partially mitigate the impact of total reflection. And the more spread ΔR is, the stronger the mitigation effect is, which is illustrated by the enlarged figures in Fig. 5 and Fig. 4 from above.

After obtaining the $\hat{\mu}$ maps using different sources and the calibration points from Case 2 in Sec. 6, we applied them individually to the energy reconstruction of positron samples listed in Tab. 2. The uniformity of the reconstructed energy E_{rec} with respect to r^3 for two different energies was plotted in Fig. 6. The two vertical lines indicate the boundaries of the three regions. Each curve is normalized by its average value within region I. The results of E_{rec} are quite consistent among the sources in region I for all positron energies, which is not surprising given that the $\hat{\mu}$ maps from different sources are almost the same. The non-uniformity in region II could be traced back to the features of the $\hat{\mu}$ maps, caused by total reflection as mentioned before. Take the bump peak in the $E_k = 5$ MeV case as an example. The corresponding radius is $r = 16.1$ m which is the same as

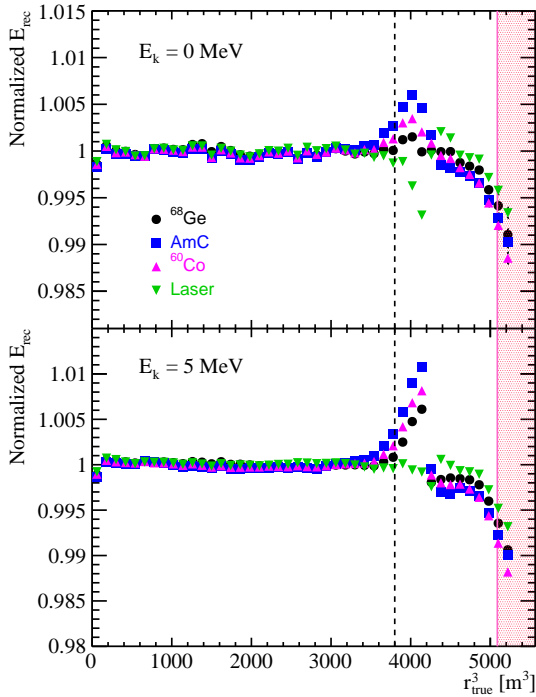


Figure 6: Uniformity of reconstructed energy E_{rec} with respect to r^3 using $\hat{\mu}$ maps from different sources. For each r^3 bin, the mean value of E_{rec} is plotted. Top and bottom plots correspond to $E_k = 0, 5$ MeV e^+ samples respectively.

the top right plot in Fig. 5. Comparing to the Laser source, the other sources will give smaller expected $\hat{\mu}$, resulting in larger E_{rec} . The size of the non-uniformity for each source is positively correlated to its ΔR spread. Another important thing we should note is that using the $\hat{\mu}$ maps from ^{68}Ge source yields the best uniformity at $E_k = 0$ MeV, while at high energies the $\hat{\mu}$ maps from Laser source perform the best.

By comparing the sources thoroughly, we aimed to pick out one that gives good energy reconstruction performance across the entire positron energy range. Based on the studies above, none of the sources is satisfactory. If one single source won't do, is it possible to use a combined source? Let us dive back to the energy deposition of positron in LS again. The whole process can be naturally broken down into two parts: almost all positrons will fully deposit their kinetic energy first, this part can be treated as a point-like source. There is a small probability that positrons will annihilate in flight, but this can be safely ignored. The second part is the positron-electron annihilation producing two gammas, which is almost the same as the ^{68}Ge source. This explains why the ^{68}Ge source performs the best for $E_k = 0$ MeV positron events. With increasing kinetic energy, positron becomes more and more point-like. Consequently point-like source such as Laser is more suitable at higher energies. Thus for positrons with visible energy E_{vis} , we

propose the following combined $\hat{\mu}^{comb}(r, \theta, \theta_{PMT})$:

$$\hat{\mu}^{comb} = \frac{1}{E_{vis}} \cdot (E_{vis}^{Ge} \cdot \hat{\mu}^{Ge}(r, \theta, \theta_{PMT}) + E_k \cdot \hat{\mu}^L(r, \theta, \theta_{PMT})) \quad (3)$$

$$E_{vis} = E_{vis}^{Ge} + E_k$$

where $\hat{\mu}^{Ge}(r, \theta, \theta_{PMT})$ and $\hat{\mu}^L(r, \theta, \theta_{PMT})$ correspond to the annihilation part and kinetic energy part of positron respectively, E_k is the kinetic energy of positron and E_{vis}^{Ge} (1.022 MeV) is the visible energy of ^{68}Ge .

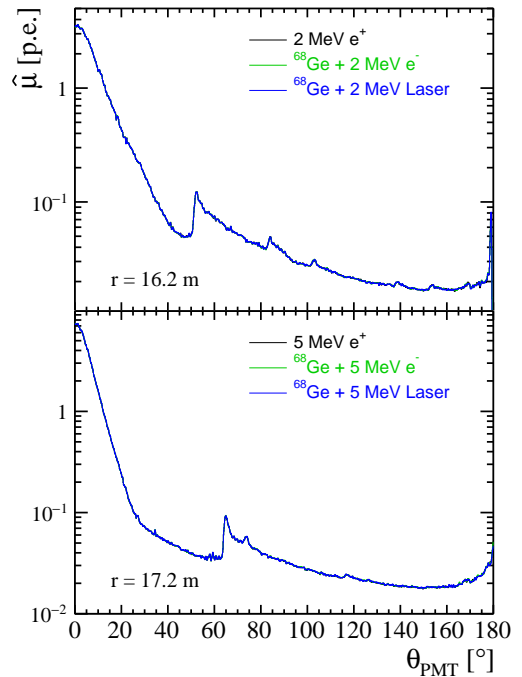


Figure 7: Validation of the combined maps $\hat{\mu}^{comb}$. Top and bottom plots are for $E_k = 2, 5$ MeV and $r = 16.2, 17.2$ m respectively. The three curves in each plot overlap with each other, confirming the correctness of the combined maps.

To validate the combined maps $\hat{\mu}^{comb}$, they were compared to those produced with positron samples listed in Tab. 2. Across the whole energy range, $\hat{\mu}^{comb}$ are able to match the positron $\hat{\mu}$ maps. A few examples are shown in Fig. 7. Note that it is assumed the kinetic energy part of the combined maps is linearly proportional to the kinetic energy. Energy non-linearity is not considered and has tiny impact on $\hat{\mu}^{comb}$. Replacing Laser with other point-like sources such as electron works as well and does not make any big difference for $\hat{\mu}^{comb}$. Laser is chosen but not electron simply due to the lack of mono-energetic electron sources in reality. For the Laser source, the emitted photons are assumed to be isotropic. In reality the non-uniformity of photon emission for the Laser source in JUNO is expected to be about a few percent. Alternative Laser samples were produced where an arbitrary 5% non-uniformity is added by hand. The resulting $\hat{\mu}^L$ maps do not change much compared with the default

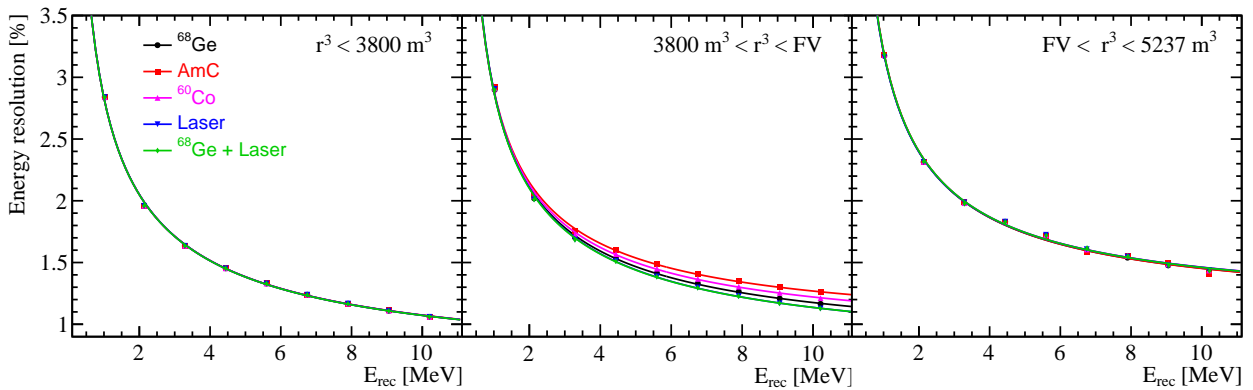


Figure 8: Comparison of the resolution of the reconstructed visible energy for positrons in the three regions of the CD. Different colors correspond to the various sources which are used to construct the $\hat{\mu}$ maps. The dots correspond to positrons with different kinetic energies. E_{rec} is the mean value of the reconstructed visible energy. Please note that energy non-linearity is not corrected here. As one can see from the middle plot, with better energy uniformity, the combined source is able to improve the energy resolution in Region II.

Laser samples, indicating that our calibration procedure is not particularly sensitive to the non-uniformity of the Laser source.

After $\hat{\mu}^{comb}$ were produced and validated, their energy reconstruction performance was evaluated as before. The energy uniformity at various energies is shown in Fig. 9, which clearly

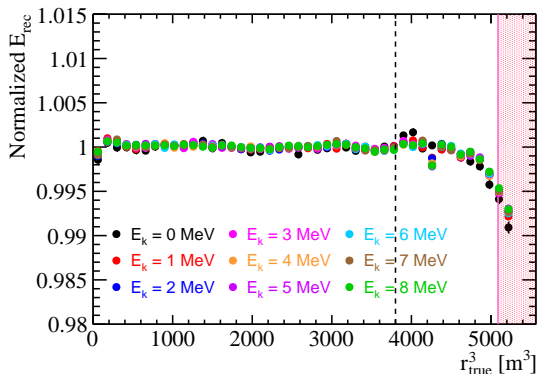


Figure 9: Uniformity of E_{rec} with respect to r^3 using combined maps $\hat{\mu}^{comb}$ at various energies. For each r^3 bin, the mean value of E_{rec} is plotted.

has very small dependence on the energy. More importantly, it is largely improved in the total reflection region comparing to Fig. 6. For each positron sample with different kinetic energy, the distribution of the reconstructed visible energy is fitted with a Gaussian function, and the corresponding energy resolution is defined as the ratio of the Gaussian sigma to the Gaussian mean. The energy resolution with respect to the mean value of the reconstructed visible energy for all the positron samples in the three regions is shown in Fig. 8. Different colors correspond to different sources that are used to produce the $\hat{\mu}$ maps. The dots represent the energy resolution at different energies. Please note that energy non-linearity is not corrected here. In regions I and III, the energy resolution is almost identical when using $\hat{\mu}$ maps from different sources. In region II, the combined maps $\hat{\mu}^{comb}$ yield the best energy resolution especially at high energies, which is a direct consequence of improved energy uni-

formity. The energy resolution is fitted with an empirical model below:

$$\frac{\sigma}{E} = \sqrt{\frac{a^2}{E} + b^2} \quad (4)$$

where a is related to the photon poisson statistics, b is the constant term and the unit of energy is MeV. The fitted results are summarized in Tab. 3. In regions I and III, there is no big dif-

Table 3: Comparison of fitted parameters for the empirical energy resolution model among various sources. The unit for a (b) is $\% \times \text{MeV}^{\frac{1}{2}}$ (%). The fit uncertainties for a and b are less than 0.005 (0.02) in regions I and II (III).

Region	I		II		III	
	a	b	a	b	a	b
AmC	2.76	0.626	2.74	0.926	3.02	1.09
^{60}Co	2.76	0.624	2.76	0.853	3.01	1.11
^{68}Ge	2.76	0.623	2.77	0.784	3.01	1.10
Laser	2.76	0.623	2.80	0.711	3.00	1.11
$^{68}\text{Ge}+\text{Laser}$	2.76	0.622	2.79	0.715	3.01	1.11

ference for a and b . But in region II, it is clear that energy non-uniformity contributes to the b term. Compared to the AmC source which has the worst non-uniformity, the combined $^{68}\text{Ge}+\text{Laser}$ source improves the b term by 22.8%.

6. Optimization of Calibration Positions

In Sec. 5 we have looked into various calibration sources and found that $^{68}\text{Ge}+\text{Laser}$ combined source is the best choice for positrons in the kinetic energy range of [0-10] MeV. In addition to the source, the number and positions of calibration points should also be carefully considered. As a simple measure of the detector energy response, the contours of total number of detected PEs on the $\theta - r^3$ plane for positron samples are drawn in Fig. 10. They clearly show that the detector energy response heavily depends on the position. Through finite

calibration points, we try to capture the features of the detector energy response and then extrapolate to all areas as accurately as possible. The better we could do this, the more we will be able to improve the energy uniformity of the detector. However the calibration points from Ref. [12], as represented by the open circles in Fig. 10, do not have enough coverage near the detector boundary and the arrangement is somewhat random. We proposed to further optimize the calibration points utilizing the contours. The arrangement could be more efficient by assigning more (less) points in areas where the detector energy response changes dramatically (slowly).

For completeness, we considered a few different scenarios:

- Case 1: mimics the ideal case with infinite calibration points. 2000 points are randomly chosen in the (r^3, θ) plane to allow more points in regions II and III
- Case 2: represents the optimal case with 275 points selected based on the contours of total number of PEs
- Case 3: corresponds to a more realistic case where those unreachable points in Case 2 are replaced with adjacent points on the CLS boundaries
- Case 4: includes additional 19 points from GT on top of Case 3

The arrangement of the calibration points on the $\theta - r^3$ plane for the above cases 2-4 are also shown in Fig. 10. The three purple curves represent the CLS boundaries and the areas they semi-enclose are not reachable. The points are the selected calibration positions. The black dots are common for Cases 2, 3 and 4. While the cross marks are for Case 2, the blue squares are for Case 3 and the red triangles are the positions from GT. Most of the selected points are at the intersections of the contours and fixed θ or r^3 lines. In areas where the contours vary rapidly, more points are assigned.

We chose the combined $^{68}\text{Ge}+\text{Laser}$ source, constructed the $\hat{\mu}$ maps for the 4 different cases above, and then compared their energy reconstruction performance. Fig. 11 shows the E_{rec} uniformity comparison at $E_k = 5$ MeV, similar results were observed at other energies given that energy uniformity has negligible energy dependence after using the combined source. Case 1 has the smallest non-uniformity. The difference between Case 1 and Case 2 is marginal, indicating that we could largely reduce the total number of calibration points without jeopardizing the reconstruction performance. After replacing those unreachable points in Case 2, the energy uniformity becomes worse for Case 3 near the detector border. The GT system is originally designed to calibrate the detector energy response near the detector border, complementary to CLS. After adding the points from the GT, the energy uniformity in Case 4 slightly improved with respect to Case 3.

The energy resolution was also compared for the four cases as shown in Fig. 12. Overall, the performance is close. Differences of energy resolution in regions II and III are consistent with the energy uniformity comparison in Fig. 11, where smaller energy non-uniformity leads to better energy resolution. The fitted energy resolution using Eqn. 4 are listed in Tab. 4.

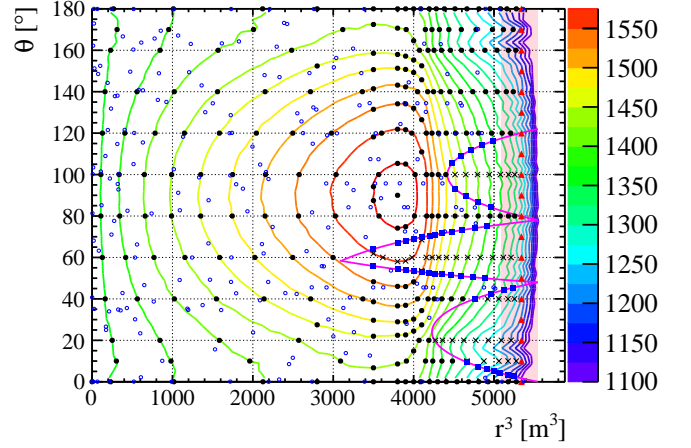


Figure 10: Contours of total number of PEs on $\theta - r^3$ plane and the arrangement of calibration points for different cases. The three purple curves represent the CLS boundaries. The open circles represent the points from Ref. [12]. The black dots are common for Cases 2, 3 and 4. While the cross marks are for Case 2, the blue squares are for Case 3 and the red triangles are the positions from GT.

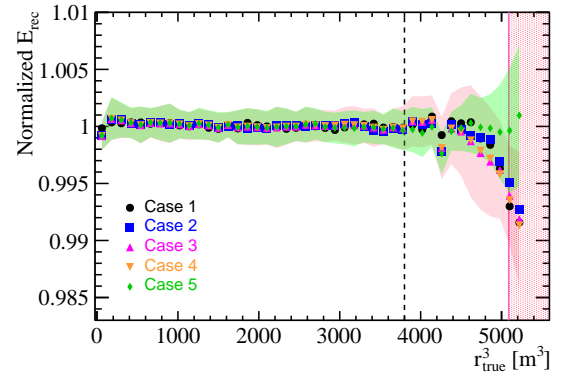


Figure 11: Uniformity of E_{rec} with respect to r^3 from different cases of calibration points at $E_k = 5$ MeV. The green and pink shadowed bands represent the 1σ variation of the E_{rec} along the θ direction for Cases 3 and 5 respectively. Case 5 will be discussed separately in Sec. 7.

The b term is larger for Case 3 compared to Case 2, and with the help of the GT, the b term was slightly reduced from Case 3 to Case 4.

Table 4: Comparison of fitted parameters for the empirical energy resolution for the five cases. The unit for a (b) is $\% \times \text{MeV}^{\frac{1}{2}}$ (%). The fit uncertainties for a and b are less than 0.005 (0.02) in regions I and II (III).

Region	I		II		III	
	a	b	a	b	a	b
Case 1	2.76	0.622	2.80	0.711	3.02	1.07
Case 2	2.76	0.622	2.79	0.715	3.01	1.11
Case 3	2.76	0.622	2.81	0.730	2.98	1.15
Case 4	2.76	0.622	2.81	0.730	3.00	1.10
Case 5	2.76	0.622	2.79	0.698	2.99	1.07

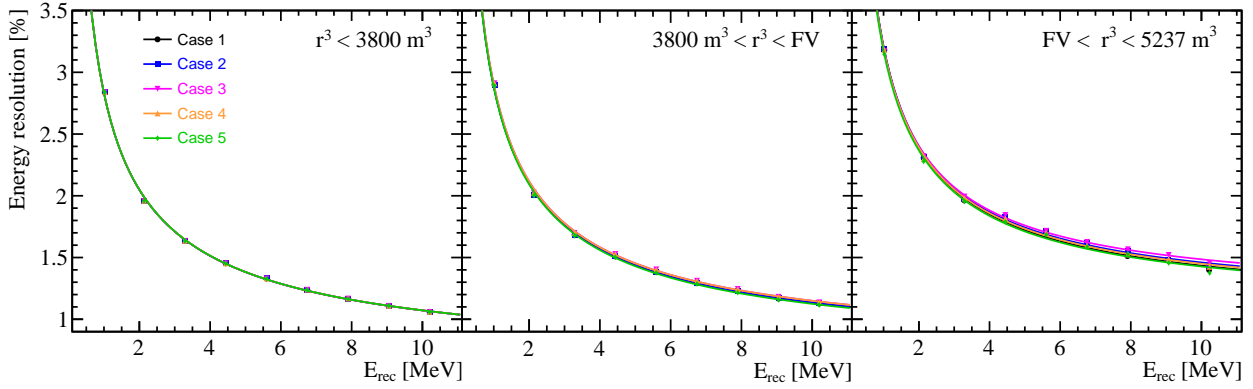


Figure 12: Comparison of the resolution of the reconstructed visible energy for positrons in the three regions of the CD. Different colors correspond to the various cases described in the text which explored the optimization of calibration positions, including azimuthal asymmetry for Case 5 discussed separately in Sec. 7. The dots correspond to positrons with different kinetic energies. E_{rec} is the mean value of the reconstructed visible energy. Please also note that energy non-linearity is not corrected here.

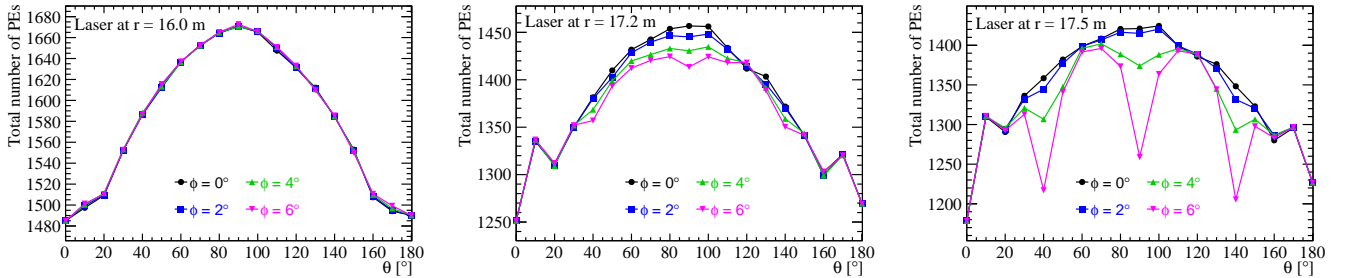


Figure 13: Comparison of the distribution of total number of PEs as a function of θ among four different ϕ planes. From left to right, the radius is fixed at $r = 16$ m, 17.2 m and 17.5 m respectively.

7. Residual Azimuthal Asymmetry

After optimizing the calibration source and positions, there is still some residual energy non-uniformity near the CD edge. While the $\hat{\mu}$ maps have already taken into account the dependence on r and θ , the ϕ dependence has not been considered due to limitation of the calibration system. To check the ϕ dependence, we compared the distribution of total number of PEs as a function of θ for two different ϕ planes at three different radius. From the left plot to the right plot in Fig. 13, one can easily see that as the position gets closer to the CD edge, the ϕ dependence becomes more and more prominent.

The CD is only approximately symmetric along the ϕ direction, since neither the PMTs nor the supporting structures have perfect azimuthal symmetry. Near the CD edge, the shadowing effect of the supporting structures can not be ignored any more. The dominant contribution comes from the numerous acrylic nodes. Although imperfect, the distribution of these acrylic nodes is roughly periodic every 6 degrees along the ϕ direction. So we can apply a ϕ dependent correction to the $\hat{\mu}$ maps within 6 degrees and extrapolate to the full ϕ range. Due to the mechanical limitation of CLS, we have to rely on MC simulation for this ϕ correction. Three ϕ planes with $\phi = 2^\circ$, 4° , 6° were selected, together with the CLS plane where $\phi = 0^\circ$, a correction function $f(\phi)$ was produced and applied to the $\hat{\mu}$ maps of

Case 3 from previous section for the edge region ($r > 15.6$ m) only. With this correction, the uniformity of E_{rec} at $E_k = 5$ MeV is plotted as Case 5 in Fig. 11. The improvement of the energy non-uniformity is outstanding in the edge region. After the correction, the residual non-uniformity is about 0.17% within the fiducial volume and 0.23% across the entire detector. The energy resolution after the correction is plotted in Fig. 12, and the fitted results are listed in Tab. 4, both referred to as Case 5. Comparing to Case 3, the improved energy uniformity propagates to the energy resolution and leads to about 4.4% and 7% decrease for the b term in regions II and III respectively.

The $f(\phi)$ correction derived above is able to reduce the residual energy non-uniformity in the CD edge region. One caveat is that this correction is derived from MC simulation, which has to be validated against real data. There are several possible ways to do this. The calibration data from GT could be used to check this correction. Another approach is to use spallation neutron events, which are abundant and uniformly distributed in the detector [20]. In the future, if we were able to reconstruct the event vertex with good precision, we could use spallation neutron events to obtain the $f(\phi)$ correction, instead of relying on MC simulation.

8. Conclusion

It is rather challenging to achieve high precision energy resolution for large LS detectors such as JUNO. Lots of studies have been done previously to address the energy uniformity utilizing calibration data in JUNO. In those studies, the residual energy non-uniformity is about 0.3% within the fiducial volume, and gets much worse near the detector boundary due to complicated optical processes like total reflections, shadowing effects of opaque materials. In this paper we expanded the $\hat{\mu}$ maps of expected PEs for PMTs to include the θ dependence. The choice of the calibration source was thoroughly investigated, and we found that $^{68}\text{Ge}+\text{Laser}$ combined source outperforms any single source across the entire energy range of interest. We also optimized the number and positions of the calibration points based on a novel strategy, which utilizes the contours of the total number of detected PEs. The small residual non-uniformity caused by the azimuthal asymmetry of the detector was handled by a ϕ dependent correction. As a result, we were able to reduce the energy non-uniformity from about 0.64% to 0.38% for regions near the detector boundary. And the energy non-uniformity within the fiducial volume (across the whole detector) could be well constrained under 0.17% (0.23%). As a direct consequence of the improved energy uniformity, better energy resolution was achieved.

Another interesting finding is that the energy non-uniformity in the central region of the detector is not particularly affected by the choice of the calibration source, nor by the asymmetry of the detector. This allows for more flexibility on the calibration strategy in this region. Moreover the detector energy response changes relatively slowly in this region so that only a small amount of calibration points are needed, which could also serve as a guideline for the calibration strategy.

In addition to the calibration sources, there will be various physics events occurring inside the LS detector as well, we should also be able to use them to obtain a better understanding of the detector response. Assuming we could select out some specific events, which are distributed across the entire detector, and have reasonably well known energy and vertex, it would be straight forward to use them to construct $\hat{\mu}$ maps to include the ϕ dependence as well. And to go one step further, if we could have huge amount of these events, we could try novel techniques such as Machine Learning to study the detector energy response. As we are entering the precision era of neutrino experiments, which demand much better energy resolution than before, every bit of improvement counts. All the ideas and methods in this paper improved the energy uniformity and consequently the energy resolution in JUNO. They could be applied to other experiments with large LS detectors.

Acknowledgements

This work was partially supported by the National Recruitment Program for Young Professionals, by the National Key R&D Program of China under Grant No. 2018YFA0404100, by the Strategic Priority Research Program of the Chinese Academy of Sciences under Grant No. XDA10010100, and by the CAS

Center for Excellence in Particle Physics (CCEPP). We would like to thank Feiyang Zhang for the useful information and discussion about the calibration systems of JUNO.

References

- [1] P. Alivisatos, S. Berridge, N. Bokor, C. Britton, W. Bryan et al, KamLAND: A Liquid scintillator anti-neutrino detector at the Kamioka site .
- [2] BOREXINO Collaboration, Science and technology of Borexino: a real-time detector for low energy solar neutrinos, *Astropart.Phys.*16 (2002) 205-234.
- [3] DOUBLE CHOOZ Collaboration, Double Chooz: A Search for the neutrino mixing angle θ_{13} , e-Print: hep-ex/0606025 [hep-ex].
- [4] DAYA BAY Collaboration, A Precision measurement of the neutrino mixing angle θ_{13} using reactor antineutrinos at Daya-Bay , e-Print: hep-ex/0701029 [hep-ex].
- [5] RENO Collaboration, RENO: An Experiment for Neutrino Oscillation Parameter θ_{13} Using Reactor Neutrinos at Yonggwang, e-Print: 1003.1391 [hep-ex].
- [6] KamLAND Collaboration, First Results from KamLAND: Evidence for Reactor Antineutrino Disappearance, *Phys. Rev. Lett.* 90 (2003) 021802.
- [7] BOREXINO Collaboration, Neutrinos from the primary proton-proton fusion process in the sun, *Nature* 512 (2014) 383-386.
- [8] DOUBLE CHOOZ Collaboration, Indication of reactor $\bar{\nu}_e$ disappearance in the double chooz experiment, *Phys. Rev. Lett.* 108 (2012) 131801.
- [9] DAYA BAY Collaboration, Observation of electron-antineutrino disappearance at daya bay, *Phys. Rev. Lett.* 108 (2012) 171803.
- [10] RENO Collaboration, Observation of reactor electron antineutrinos disappearance in the reno experiment, *Phys. Rev. Lett.* 108 (2012) 191802.
- [11] JUNO Collaboration, Neutrino physics with JUNO, *Journal of Physics G: Nuclear and Particle Physics* 43 (2016) 030401.
- [12] JUNO collaboration, Calibration Strategy of the JUNO Experiment, arXiv:2011.06405.
- [13] W. Wu, M. He, X. Zhou, H. Qiao, A new method of energy reconstruction for large spherical liquid scintillator detectors, *Journal of Instrumentation* 14 (03) (2019) P03009–P03009.
- [14] T. Lin, J. Zou, W. Li, Z. Deng, X. Fang, G. Cao, X. Huang, and Z. You, The application of SNiPER to the JUNO simulation, *Journal of Physics: Conference Series* 898 (2017) 042029.
- [15] Agostinelli S et al. (GEANT4), GEANT4—a simulation toolkit, *Nucl. Instrum. Meth. A* 506 (2003) 250-303.
- [16] A. Abusleme et al. (JUNO Collaboration), Optimization of the JUNO liquid scintillator composition using a Daya Bay antineutrino detector, arxiv:2007.00314.
- [17] X. Zhou et al., Rayleigh scattering of linear alkylbenzene in large liquid scintillator detectors, *Rev Sci Instrum.* 86(7) (2015) 073310.
- [18] Y. Zhang et al., A complete optical model for liquid-scintillator detectors, *Nucl. Instrum. Meth. A* 967 (2020) 163860.
- [19] Y. Zhang et al., Laser calibration system in JUNO, *JINST* 14 (2019) P01009.
- [20] Daya Bay Collaboration, Measurement of electron antineutrino oscillation based on 1230 days of operation of the Daya Bay experiment, *Phys.Rev.D* 95 (2017) 7, 072006